4. J. Spencer, N. Wormald, *Combinatorica* **27**, 587 (2007).
5. A. Beveridge, T. Bohman, A. Frieze, O. Pikhurko, *Proc. Am. Math. Soc.* **135**, 3061 (2007).
6. M. Krivelevich, E. Lubetzky, B. Sudakov, "Hamiltonicity thresholds in Achlioptas processes"; available at http://arxiv.org/abs/0804.4707 (2008).
7. M. E. J. Newman, R. M. Ziff, *Phys. Rev. E Stat. Nonlin. Soft Matter Phys.* **64**, 016706 (2001).
8. We thank Microsoft Research, where our collaboration initiated, for its support. D.A. is supported in part by NSF CAREER award CCF-0546900, an Alfred P. Sloan Fellowship, and IDEAS grant 210743 from the European Research Council.

28 October 2008; accepted 16 January 2009
10.1126/science.1167782

The Initial Stages of Template-Controlled $CaCO_3$ Formation Revealed by Cryo-TEM

Emilie M. Pouget,[1,2] Paul H. H. Bomans,[1,2] Jeroen A. C. M. Goos,[1] Peter M. Frederik,[2,3] Gijsbertus de With,[1,2] Nico A. J. M. Sommerdijk[1,2]*

Biogenic calcium carbonate forms the inorganic component of seashells, otoliths, and many marine skeletons, and its formation is directed by an ordered template of macromolecules. Classical nucleation theory considers crystal formation to occur from a critical nucleus formed by the assembly of ions from solution. Using cryotransmission electron microscopy, we found that template-directed calcium carbonate formation starts with the formation of prenucleation clusters. Their aggregation leads to the nucleation of amorphous nanoparticles in solution. These nanoparticles assemble at the template and, after reaching a critical size, develop dynamic crystalline domains, one of which is selectively stabilized by the template. Our findings have implications for template-directed mineral formation in biological as well as in synthetic systems.

In nature, hybrid materials consisting of a combination of soft organic and hard inorganic components are used for a variety of purposes, including mechanical support, navigation, and protection against predation (*1*, *2*). These biominerals, such as bones, teeth, and shells, often combine fascinating shapes with remarkable mechanical (*3*) and optical (*4*) properties, which generally are related to a high level of control over structure, size, morphology, orientation, and assembly of the constituents.

Calcium carbonate is the most abundant crystalline biomineral. In nature, its formation generally takes place in specialized, self-assembled compartments, such as vesicles or layered macromolecular structures, where domains of acidic proteins induce oriented nucleation (*5*, *6*). Avoiding the complexity and dynamics of the biological mineralization systems, template-directed $CaCO_3$ mineralization has been studied in vitro through the use of two-dimensional (2D) molecular assemblies as model systems (*7*).

According to classical nucleation theory, the crystallization of inorganic minerals starts from their constituting ions, which, on the basis of their ionic complementarity, form small clusters in a stochastic process of dynamic growth and disintegration (*8*). These clusters become stable when a critical size is reached at which the increasing surface energy related to the growing surface area is balanced by the reduction of bulk energy related to the formation of a crystal lattice. The resulting primary nanoparticles form the critical crystal nuclei that are the basis of further growth through the associated reduction of the Gibbs free energy of the system.

In contrast to what is described by classical nucleation theory, calcium carbonate crystal formation has been shown to occur from a transient amorphous precursor phase, both in biological (*9*, *10*) and in biomimetic systems (*11*, *12*). Moreover, it was recently shown that $CaCO_3$ nucleation (*13*) is preceded by the formation of nanometer-sized prenucleation clusters, which also is not foreseen by classical nucleation theory. Although a recent model described how a template can direct orientated nucleation from an amorphous calcium carbonate (ACC) precursor phase (*14*), the role of prenucleation clusters in template-directed mineralization is still unknown.

Previously, with the use of a vitrification robot and attached glovebox, we were able to load a self-organized monolayer with adhered mineralization solution onto a holey carbon cryotransmission electron microscopy (cryo-TEM) grid with minimal disturbance of the system while maintaining 100% humidity and constant temperature (fig. S1) (*11*, *15*). Plunge-freeze vitrification of the sample at various time points allowed trapping of the different stages of the mineralization reaction and monitoring of the development of the mineral phase in its native hydrated state by cryo-TEM. Using 2D imaging and diffraction, we showed the formation of a transient ACC phase and demonstrated its transformation into oriented vaterite before the formation of the final product, oriented calcite. However, this study did not show which steps in the mineralization process depended critically on the presence of the monolayer, nor did it discover the prenucleation clusters.

The present work used a stearic acid monolayer as a template deposited on a supersaturated 9 mM $Ca(HCO_3)_2$ solution (*16*). We studied the system through a combination of cryoelectron tomography (cryo-ET) (*17*) and low-dose selected-area electron diffraction (SAED), obtaining morphological and structural information with 3D spatial resolution. This allowed us to image, locate, and identify $CaCO_3$ nanoparticles in solution and to establish whether they were actually in contact with the template. Also, by using high-resolution cryo-TEM, we could visualize prenucleation clusters and collect evidence for their role in the nucleation of the amorphous nanoparticles. Tomography revealed that these particles nucleated in solution but later assembled at the template surface, where crystallinity developed; low-dose SAED showed selective stabilization of single crystallographic orientation through the interaction of the mineral with the monolayer.

High-resolution cryo-TEM studies of fresh 9 mM $Ca(HCO_3)_2$ solutions showed prenucleation clusters with dimensions of 0.6 to 1.1 nm (Fig. 1, A and B). At the same time, a small population of larger clusters (<4 nm) was detected (Fig. 1C, inset), indicating the onset of the aggregation process leading to nucleation. After reaction times of 2 to 6 min, small nanoparticles with a size distribution centered around 30 nm were observed (Fig. 2A).

Samples were taken from the crystallization solution at different time points (figs. S2 and S3) (*15*) and analyzed with analytical ultracentrifugation, which detects species in solution according to the difference in their sedimentation coefficient s (*18*). Large and dense particles sediment faster than smaller or less dense particles, thereby yielding a higher value of s. These experiments confirmed the presence of nanoclusters ($s = 1.5 \times 10^{-13}$ to 3×10^{-13} s) coexisting with ions ($s \leq 0.6 \times 10^{-13}$ s), followed by the aggregation of the clusters ($s \geq 4.5 \times 10^{-13}$ s) before the nucleation event.

Gebauer *et al.* (*13*) provided convincing evidence that the existence of prenucleation clusters is due to thermodynamic equilibrium among solvent, individual hydrated ions, and hydrated clusters, as represented by

$$z\{Ca^{2+}\}_{aq} + z\{CO_3^{2-}\}_{aq} \leftrightarrow \{CaCO_3\}_{z,aq} \quad (1)$$

in which the clusters are considered as a solute entity and z is the number of $CaCO_3$ units in a cluster. In the absence of data on prenucleation cluster concentrations, and a value for z, quantitative assessment is currently not possible. They speculated that the release of water molecules from the hydration shell of ions provides a substantial entropy gain favoring prenucleation cluster formation.

Low-dose SAED showed that the 30-nm nanoparticles were amorphous, and cryo-ET dem-

[1]Laboratory of Materials and Interface Chemistry, Eindhoven University of Technology, P.O. Box 513, 5600 MB Eindhoven, Netherlands. [2]SoftMatter CryoTEM Unit, Eindhoven University of Technology, P.O. Box 513, 5600 MB Eindhoven, Netherlands. [3]EM Unit, Department of Pathology, University of Maastricht, Universiteitssingel 50, 6229 ER Maastricht, Netherlands.

*To whom correspondence should be addressed. E-mail: n.sommerdijk@tue.nl

onstrated that they were present throughout the whole solution (Fig. 2, A, D, and E) (*15*), implying that their formation is independent of the presence of the organic template. The SAED patterns obtained from the ACC particles and the fresh $Ca(HCO_3)_2$ solutions were indistinguishable and were clearly different from vitrified films of pure water and aqueous 10 mM $CaCl_2$ solutions (Fig. 1D). The similarities and differences among the different samples are not only immediately clear from the position of the second diffraction ring [at 4.61 ± 0.05 Å for ACC and 9 mM $Ca(HCO_3)_2$; at 4.82 ± 0.05 Å and 4.90 ± 0.05 Å for water and 10 mM $CaCl_2$, respectively], but are also statistically significant in the maximum of the first diffraction ring (tables S1 and S2) (*15*). These results suggest that the prenucleation clusters present in freshly prepared $Ca(HCO_3)_2$ solutions consist of ACC.

In contrast to the observations of Gebauer *et al.* (*13*), our experiments showed that the prenucleation clusters persisted after nucleation. We speculate that the formation of the ~30-nm nanoparticles is due to aggregation of the prenucleation clusters via Brownian motion. Considering that the prenucleation clusters already have the structure of the ACC particles found after nucleation, the aggregation of clusters mainly leads to a gain in surface enthalpy. We consider this to be the main driving force for stabilization of the ACC nanoparticles. However, it is noteworthy that experiments (*19*) and simulations (*20*) have indicated that $CaCO_3$ domains with sizes of ≤2 nm may already possess short-range local order.

After longer reaction times (10 to 20 min), larger particles with sizes ranging from 70 to 250 nm were observed (Fig. 2, B, D, and F) in coexistence with a persistent population of the ~30-nm nanoparticles. Tomograms showed that the larger particles were found exclusively at the interface with the monolayer and that all exhibited a smooth face interacting with the template. Low-dose SAED revealed that some of these were still amorphous (Fig. 2D, particle 2), whereas others produced complex spot patterns (Fig. 2D, particles 3 to 5) that could be assigned to vaterite displaying multiple crystallographic orientations (fig. S4) (*15*). The template-associated amorphous particles were larger than those found in solution and had a size range of 70 to 120 nm, which implies that these are temporarily stabilized by the monolayer. The particles in which crystallinity had developed were found in all sizes (70 to 250 nm), which suggests that in the present system the size of ~120 nm is a critical upper limit for the stability of the amorphous phase. Conversely, the observations that most ACC particles have a size of <70 nm, whereas polycrystalline $CaCO_3$ has a minimal particle diameter of ~70 nm, imply that this size is critical for the development of crystalline domains inside an amorphous matrix.

The size of the particles further increased, and an increasing fraction of these particles showed a dominating or even a single diffraction pattern (particle diameters of >300 nm) (Fig. 2, F and G, and fig. S4) (*15*). In accordance with literature (*16*, *21*, *22*), SAED identified this plane as (00.1) vaterite (Fig. 2, C and D); in the absence of a monolayer, a mixture of randomly oriented calcite and vaterite was obtained (fig. S6) (*15*). Tomograms showed that after a reaction period of 30 to 60 min, the nanoparticles were still present throughout the solution, and in many cases they were found to decorate the surface of the 300- to 500-nm vaterite crystals (Fig. 2G).

In accordance with electron microscopy observations (*9*, *14*) and simulations (*23*), the present results imply a locally confined transformation of the amorphous to the crystalline state. Also, structural and spectroscopic techniques have demonstrated the development of short-range order in transient ACC, indicating a gradual development of crystallinity within the material (*24*, *25*). None-

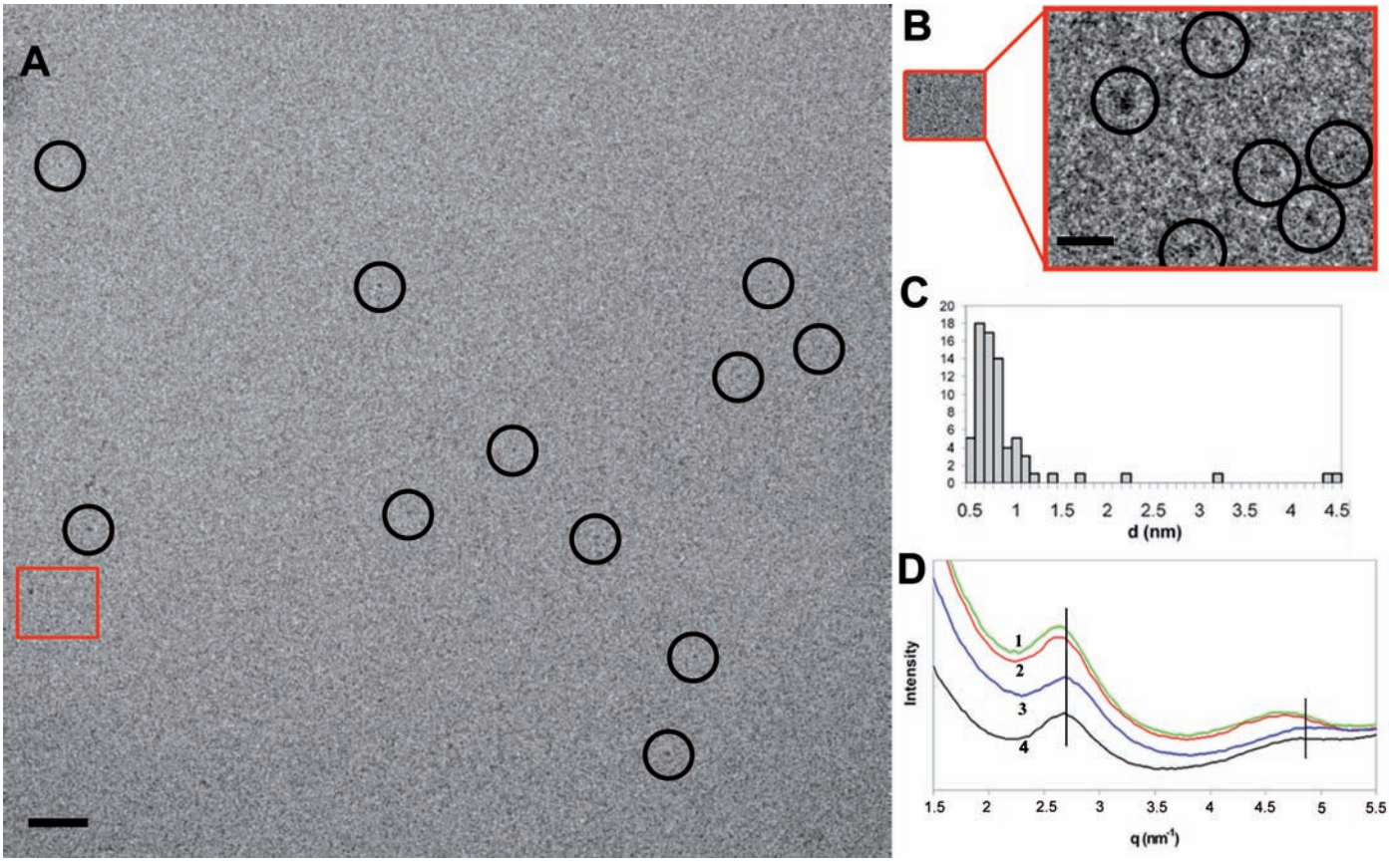

Fig. 1. (**A**) High-resolution cryo-TEM image of a fresh 9 mM $Ca(HCO_3)_2$ solution after image processing (*15*) in which prenucleation clusters are observed. An arbitrary number of clusters are highlighted by black circles. Scale bar, 20 nm. (**B**) Nonfiltered images representing the zone delimited by the red square in (A). In the high-magnification image, all particles present are highlighted by black circles. Particle sizes below the detection limit of 0.45 nm (3 times the pixel size) are considered noise. Scale bar, 5 nm. (**C**) Particle diameter (*d*) distribution of the prenucleation clusters observed in the cryo-TEM images. (**D**) Radial integration of the diffraction patterns of vitrified aqueous solutions of (1) ACC (green), (2) 9 mM $Ca(HCO_3)_2$ (red), (3) water (blue), and (4) 10 mM $CaCl_2$ (black). Vertical (black) lines are drawn to indicate the shifts of the diffraction rings of the different samples with respect to that of a vitrified film of pure water.

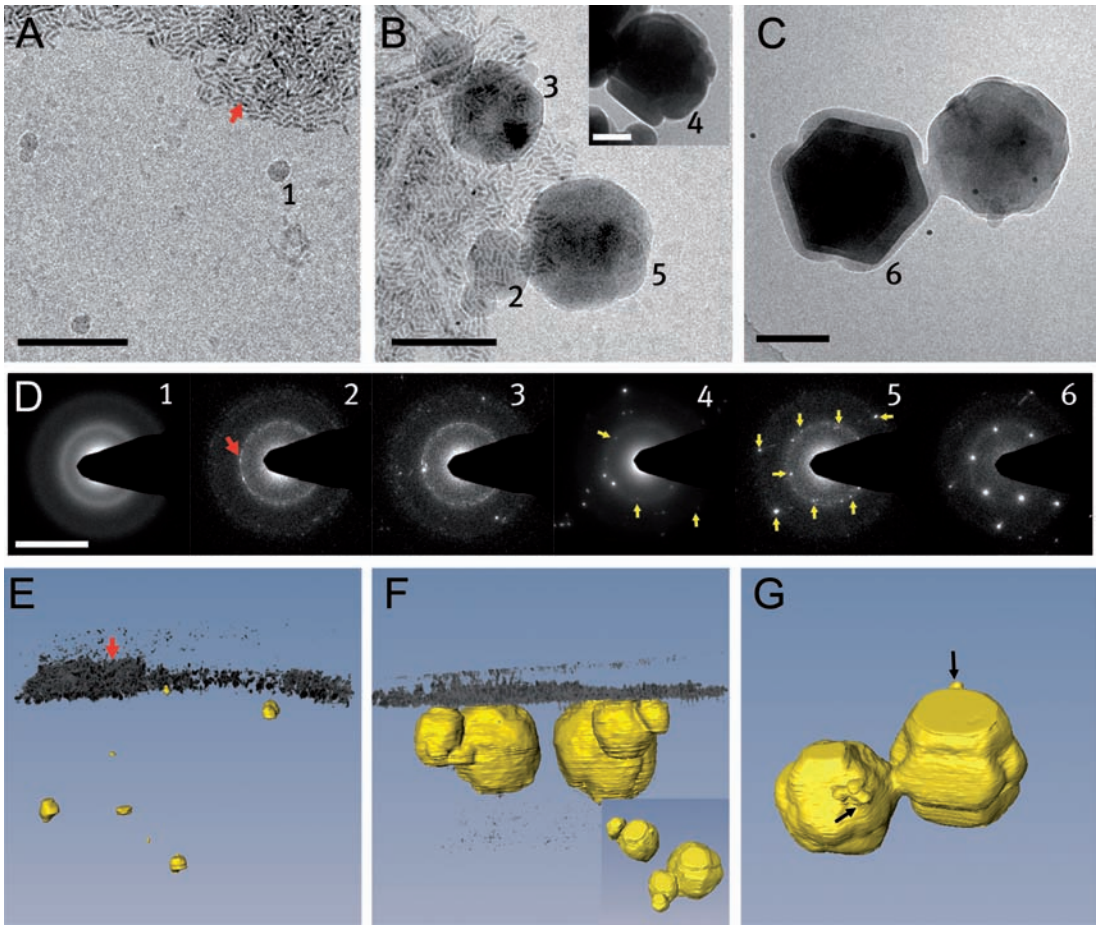

Fig. 2. (**A** to **C**) Cryo-TEM images of the early, intermediate, and mature stages, after reaction times of 6 min, 11 min, and 45 min, respectively. Inset in (B) is a micrograph taken from a different area. Scale bars, 200 nm. (**D**) Diffraction patterns of the particles marked in (A) to (C), showing the development of crystallinity during the mineralization. Scale bar, 5 nm^{-1}. Particles 1 and 2 are amorphous; particles 3 to 5 are polycrystalline. The marked spots can be indexed (yellow arrows) as vaterite oriented (00.1). The *d*-spacings of the other spots fit with the vaterite distances. Particle 6 is vaterite (00.1). See details of the diffraction pattern indexation in (*15*). (**E** to **G**) Computer-aided visualization of the tomograms recorded from the areas shown in (A) to (C) (*15*). The red arrows in (E) show the nanorods marking the monolayer (fig. S5) (*15*). The black arrows in (G) show the 30-nm ACC decorating the more mature crystals. Inset in (F) shows the particle surfaces that interact with the monolayer.

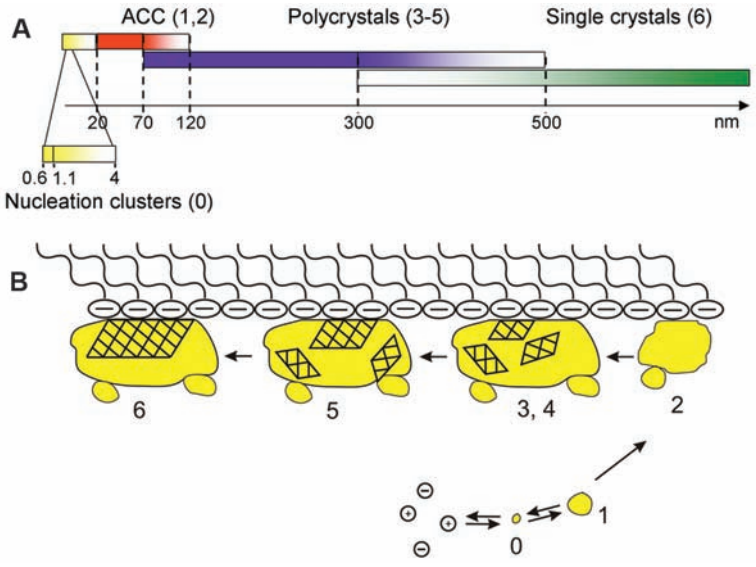

Fig. 3. The different stages of template-controlled calcium carbonate formation. (**A**) The distribution of particle diameters at different stages of crystal development. (**B**) Schematic pathway of the mineralization of an organic matrix. Step 0: formation of prenucleation clusters. Step 1: Aggregation of the clusters to form 30-nm ACC nanoparticles. Step 2: Clustering and growth of the ACC particles at the surface of the organic matrix. Step 3: Start of the crystallization; formation of poorly crystalline particles. Step 4: Formation of nanocrystalline domains inside the amorphous particle. Step 5: Prevalent growth of the crystalline domain stabilized by the template. Step 6: Formation and growth of oriented single crystals. Numbers in parentheses in (A) and step numbers in (B) relate to the particle numbers in Fig. 2.

theless, for several other calcium carbonate–based systems, crystallization proceeds through a dissolution-reprecipitation mechanism (*12*, *26*). Moreover, we cannot exclude the possibility that the presence of water mediates this phase transformation through the solubilization of ACC on a nanoscopic scale (*19*).

The narrow size distribution of the initial ACC particles suggests an optimal stability at a diameter of ~30 nm, similar to previous reports for mineral nanoparticles in studies of calcium carbonate from nacre (*6*) and calcium phosphate from enamel (*27*). The presence of these nanoparticles in all stages of the mineral formation process (fig. S8) (*15*) supports proposals that these nanoparticles form the feedstock on which the larger particles and crystals grow (*11*, *28*). Although the observation that nanoparticles adhere to the surface of the vaterite crystals (Fig. 2G) suggests that growth proceeds through the direct addition of such particles, no crystals with roughened surfaces have been observed. Therefore, also considering the high solubility of ACC in water (1.7 mM) (*29*), one may expect that the nanoparticles exist in equilibrium with the material in solution, and we propose that the growth of the larger particles occurs through a dissolution-reprecipitation mechanism at the expense of the nanoparticles (*30*).

We propose that the template-directed crystallization of $CaCO_3$ proceeds through several distinct steps (Fig. 3) (*15*). The starting point is

the formation of prenucleation clusters with dimensions of 0.6 to 1.1 nm (step 0). In analogy to the chemistry of calcium phosphate (*31*), we consider them to be the smallest stable agglomerates of $CaCO_3$ present from the beginning of the reaction. Aggregation of these clusters in solution leads to the nucleation of ACC nanoparticles with a size distribution centered around 30 nm (step 1). Association of these particles with the template surface initiates the growth of ACC (step 2), using the nanoparticles in their neighborhood as feedstock. Next, randomly oriented nanocrystalline domains are formed inside the otherwise amorphous particles (steps 3 and 4). On the basis of the model of Zhang *et al*. (*23*), we expect these domains to be unstable and in equilibrium with the amorphous phase. In the last steps, the orientation that is stabilized through the interaction with the monolayer becomes dominant (step 5) and develops into a single crystal (step 6). This single crystal probably grows by the further addition and incorporation of ions and clusters from solution.

The initial experiments of Mann and co-workers showed that the present system could produce calcite ($1\bar{1}.0$) or vaterite (00.1) depending on the precise conditions (*16*, *32*). Later, it was demonstrated that rapid CO_2 evaporation favors the kinetic product, vaterite (*21*, *22*), whereas lower evaporation rates lead to the calcitic form (*21*). These results are confirmed by our finding of (00.1) oriented vaterite in the present work (i.e., in a fast-outgassing thin film) and the formation of ($1\bar{1}.0$) oriented calcite in crystallization dishes (fig. S7) (*15*) from which CO_2 outgassing is slower. Moreover, the observation of randomly oriented vaterite crystals also puts in perspective the synchrotron x-ray scattering experiments that showed the formation of randomly oriented crystals from the same system (*22*).

The nanoscopic prenucleation clusters that we visualized are the smallest stable form of $CaCO_3$ and are likely the building blocks of the amorphous precursor particles observed in biomineralization; such particles are also observed in many synthetic systems and are not restricted to calcium carbonate (*13*, *31*). As a consequence of their aggregation, ACC nucleates in solution and subsequently assembles at the template. There, it is present as a temporarily stabilized but transient phase that mediates the transfer of information from the template to the mineral phase. This occurs through the selective stabilization of only one of the orientations present, leading to the development of a single crystal.

References and Notes

1. H. A. Lowenstam, S. Weiner, *On Biomineralization* (Oxford Univ. Press, New York, 1989).
2. M. E. Davis, *Science* **305**, 480 (2004).
3. B. L. Smith *et al*., *Nature* **399**, 761 (1999).
4. J. Aizenberg *et al*., *Science* **309**, 275 (2005).
5. J. R. Young, J. M. Didimus, P. R. Bown, B. Prins, S. Mann, *Nature* **356**, 516 (1992).
6. L. Addadi, D. Joester, F. Nudelman, S. Weiner, *Chem. Eur. J.* **12**, 980 (2006).
7. N. A. J. M. Sommerdijk, G. de With, *Chem. Rev.* **108**, 4499 (2008).
8. M. Volmer, *Kinetik der Phasenbildung* (Steinkopff, Dresden, 1939).
9. Y. Politi, T. Arad, E. Klein, S. Weiner, L. Addadi, *Science* **306**, 1161 (2004).
10. E. Beniash, J. Aizenberg, L. Addadi, S. Weiner, *Proc. R. Soc. London Ser. B* **264**, 461 (1997).
11. B. P. Pichon, P. H. H. Bomans, P. M. Frederik, N. A. J. M. Sommerdijk, *J. Am. Chem. Soc.* **130**, 4034 (2008).
12. J. R. I. Lee *et al*., *J. Am. Chem. Soc.* **129**, 10370 (2007).
13. D. Gebauer, A. Völkel, H. Cölfen, *Science* **322**, 1819 (2008).
14. C. L. Freeman, J. H. Harding, D. M. Duffy, *Langmuir* **24**, 9607 (2008).
15. See supporting material on *Science* Online.
16. S. Mann, B. R. Heywood, S. Rajam, J. D. Birchall, *Nature* **334**, 692 (1988).
17. S. Nickell, C. Kofler, A. P. Leis, W. Baumeister, *Nat. Rev. Mol. Cell Biol.* **7**, 225 (2006).
18. The sedimentation coefficient *s* is defined as the velocity v_t of the particle per unit gravitational acceleration (centrifugal acceleration: $\omega^2 r$, where ω is angular velocity and *r* is the radial distance to the rotation axis).
19. F. M. Michel *et al*., *Chem. Mater.* **20**, 4720 (2008).
20. D. Quigley, P. M. Rodger, *J. Chem. Phys.* **128**, 221101 (2008).
21. E. Loste, E. Diaz-Marti, A. Zarbakhsh, F. C. Meldrum, *Langmuir* **19**, 2830 (2003).
22. E. DiMasi, M. J. Olszta, V. M. Patel, L. B. Gower, *CrystEngComm* **5**, 346 (2003).
23. T. H. Zhang, X. Y. Liu, *J. Am. Chem. Soc.* **129**, 13520 (2007).
24. Y. Politi *et al*., *Adv. Funct. Mater.* **16**, 1289 (2006).
25. R. S. K. Lam, J. M. Charnock, A. Lennie, F. C. Meldrum, *CrystEngComm* **9**, 1226 (2007).
26. J. Aizenberg, D. A. Muller, J. L. Grazul, D. R. Hamann, *Science* **299**, 1205 (2003).
27. R. Tang *et al*., *Angew. Chem. Int. Ed.* **43**, 2697 (2004).
28. G. Luquet, F. Marin, *C. R. Palevol* **3**, 515 (2004).
29. L. Brecevic, A. E. Nielsen, *J. Cryst. Growth* **98**, 504 (1989).
30. J. J. J. M. Donners, B. R. Heywood, E. W. Meijer, R. J. M. Nolte, N. A. J. M. Sommerdijk, *Chem. Eur. J.* **8**, 2561 (2002).
31. A. S. Posner, F. Betts, *Acc. Chem. Res.* **8**, 273 (1975).
32. S. Rajam *et al*., *J. Chem. Soc. Faraday Trans.* **87**, 727 (1991).

33. Supported by the European Community (project code NMP4-CT-2006-033277) and the Netherlands Organization for Scientific Research (NWO). We thank A. Völkel and H. Cölfen for performing and evaluating the ultracentrifugation measurements; D. Gebauer and A. Verch for time-dependent solution composition determination of the mineralization solutions; F. L. Boogaard, E. J. Creusen, J. J. van Roosmalen, and P. Moeskops for their contribution to the 3D reconstructions of the tomograms; and P. T. K. Chin for providing the CdSe nanorods.

Supporting Online Material

www.sciencemag.org/cgi/content/full/323/5920/1455/DC1
Materials and Methods
SOM Text
Table S1
Figs. S1 to S7

5 December 2008; accepted 30 January 2009
10.1126/science.1169434

but they still suffer from mechanical damage. We report the development of polyurethane networks that exhibit self-repairing characteristics upon exposure to ultraviolet light. The network consists of an oxetane-substituted chitosan precursor incorporated into a two-component polyurethane. Upon mechanical damage of the network, four-member oxetane rings open to create two reactive ends. When exposed to ultraviolet light, chitosan chain scission occurs, which forms crosslinks with the reactive oxetane ends, thus repairing the network. These materials are capable of repairing themselves in less than an hour and can be used in many coatings applications, ranging from transportation to packaging or fashion and biomedical industries.

When a hard or sharp object hits a vehicle, it is likely that it will leave a scratch, and for this reason the automotive industry looks for coatings with high scratch resistance. Because of their hardness and elasticity, polyurethanes exhibit good scratch resistance but can still suffer from mechanical damage. An ideal automotive coating would mend itself while a vehicle is driven. To heal mechanical damage in plants, suberin, tannins, phenols, or nitric oxide are activated to prevent further lesions (*1*–*3*), whereas in a human skin, the outer flow of blood cells is arrested by the crosslink network of fibrin, giving rise to wound-healing (*4*, *5*). Concentration gradients or stratification in living organisms inspired the development of spatially heterogeneous remendable polymers (*6*, *7*), composites containing micro-encapsulated spheres (*8*–*11*), encapsulated fibers (*12*–*14*), reversible cross-linking (*15*, *16*), and microvascular networks (*17*). One example is epoxy matrices containing a glass hollow fiber filled with a monomer and an initiator with the "bleeding" ability to heal polymer networks during crack formation (*12*). A similar phenomenon was used in another approach, in which a micro-encapsulated dicyclopentadiene monomer was introduced in a catalyst-embedded polymer matrix, which healed the crack near the ring opening of the monomer (*8*–*11*). Reversibility of Diels-Alder reactions resulted in another approach to thermally repair damaged areas, and approach using malemide-furan adducts (*15*, *16*). Mimicking of microvascular structures (*17*), water-responsive expandable gels (*7*), and formation of supramolecular assemblies (*18*) are other avenues of remendability.

This study departs from previous approaches and reports the development of heterogeneous

School of Polymers and High Performance Materials, Shelby F. Thames Polymer Science Research Center, The University of Southern Mississippi, Hattiesburg, MS 39406, USA.

*To whom correspondence should be addressed. E-mail: marek.urban@usm.edu